International Journal of Pharmaceutics 652 (2024) 123764

Contents lists available at ScienceDirect

International Journal of Pharmaceutics

journal homepage: www.elsevier.com/locate/ijpharm

A PEG-assisted membrane coating to prepare biomimetic mesoporous silicon for PET/CT imaging of triple-negative breast cancer

Huang Wen [a], María Gómez Martínez [b], Emilia Happonen [a], Jing Qian [a], Vanessa Gómez Vallejo [b], Helena Jorge Mendazona [b], Kimmo Jokivarsi [c], Mauro Scaravilli [d], Leena Latonen [e], Jordi Llop [b], Vesa-Pekka Lehto [a,*], Wujun Xu [a,*]

[a] Department of Technical Physics, University of Eastern Finland, Yliopistonranta 1F, 70211 Kuopio, Finland
[b] Center for Cooperative Research in Biomaterials (CIC biomaGUNE), Basque Research and Technology Alliance (BRTA), Paseo de Miramon 194, 20014 Donostia-San Sebastián, Spain
[c] A.I. Virtanen Institute for Molecular Sciences, University of Eastern Finland, Neulaniementie 2, 70211 Kuopio, Finland
[d] Faculty of Medicine and Health Technology, Tampere University, Arvo Ylpön Katu 34, 33520 Tampere, Finland
[e] School of Medicine, University of Eastern Finland, Yliopistonranta 1F, 70211 Kuopio, Finland

ARTICLE INFO

Keywords:
PEGylation
cancer cell membrane coating
mesoporous silicon
PET/CT imaging
89Zr
triple-negative breast cancer

ABSTRACT

Triple-negative breast cancer (TNBC) diagnosis remains challenging without expressing critical receptors. Cancer cell membrane (CCm) coating has been extensively studied for targeted cancer diagnostics due to attractive features such as good biocompatibility and homotypic tumor-targeting. However, the present study found that widely used CCm coating approaches, such as extrusion, were not applicable for functionalizing irregularly shaped nanoparticles (NPs), such as porous silicon (PSi). To tackle this challenge, we proposed a novel approach that employs polyethylene glycol (PEG)-assisted membrane coating, wherein PEG and CCm are respectively functionalized on PSi NPs through chemical conjugation and physical absorption. Meanwhile, the PSi NPs were grafted with the bisphosphonate (BP) molecules for radiolabeling. Thanks to the good chelating ability of BP and homotypic tumor targeting of cancer CCm coating, a novel PSi-based contrast agent (CCm-PEG-^{89}Zr-BP-PSi) was developed for targeted positron emission tomography (PET)/computed tomography (CT) imaging of TNBC. The novel imaging agent showed good radiochemical purity (~99 %) and stability (~95 % in PBS and ~99 % in cell medium after 48 h). Furthermore, the CCm-PEG-^{89}Zr-BP-PSi NPs had efficient homotypic targeting ability *in vitro* and *in vivo* for TNBC. These findings demonstrate a versatile biomimetic coating method to prepare novel NPs for tumor-targeted diagnosis.

1. Introduction

Approximately 2.6 million new cases of breast cancer (BC) were diagnosed in 2020, with 685,000 deaths worldwide (Sung et al., 2021). As a subtype of BC, triple-negative breast cancer (TNBC) has many characteristics, such as the lack of expression of estrogen and progesterone receptors, causing a challenge in cancer diagnosis and therapy (Park et al., 2018). The current diagnosis of TNBC mainly relies on tissue biopsy, although the diagnosis results are subject to sampling errors and invasiveness (Chudgar and Mankoff, 2017). Therefore, there is an urgent medical demand to develop sensitive and efficient tumor-targeting imaging approaches for the diagnosis of TNBC.

The combination of positron emission tomography (PET) and computed tomography (CT) has the advantages of unlimited penetration depth and high sensitivity, constituting an ideal approach for diagnosing cancer. In this context, nanomaterial-based nuclear imaging agents with longer blood circulation times than small molecule-based agents could result in improved diagnostic agents (Pellico et al., 2021). In particular, porous silicon (PSi) nanoparticles (NPs) are widely used in biomedical research and have unique features for PET/CT imaging for different reasons (Godin et al., 2010). First, PSi NPs are biodegradable and bioabsorbable. Second, orthosilicic acid, as the degradation product of PSi, is nontoxic and beneficial for bone growth (Jugdaohsingh et al., 2004). Third, PSi NPs have a high surface area beneficial for grafting chelators for radioisotopes in high amounts, which can subsequently be used to anchor radiometals via the formation of metal-chelator complexes. Over

* Corresponding authors.
E-mail addresses: vesa-pekka.lehto@uef.fi (V.-P. Lehto), wujun.xu@uef.fi (W. Xu).

https://doi.org/10.1016/j.ijpharm.2023.123764
Received 27 April 2023; Received in revised form 27 November 2023; Accepted 31 December 2023
Available online 2 January 2024

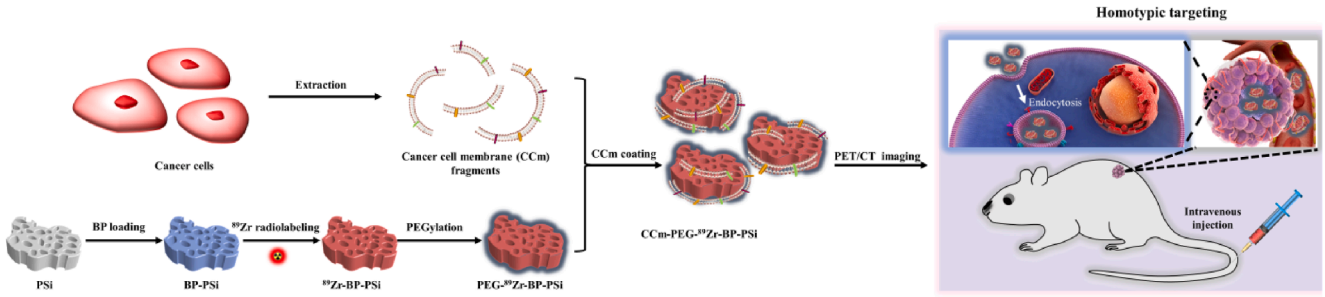

Scheme 1. Schematic illustration of preparation and application of cell membrane-coated biomimetic NPs for homotypic tumor-targeting: porous silicon (PSi); bisphosphonate loading (BP-PSi); ^{89}Zr radiolabeling (^{89}Zr-BP-PSi); PEGylation (PEG-^{89}Zr-BP-PSi) and cancer cell membrane coating (CCm-PEG-^{89}Zr-BP-PSi).

the past few years, PSi has been radiolabeled with various isotopes, such as ^{111}In (Ferreira et al., 2016; Ferreira et al., 2017; Lumen et al., 2021), ^{18}F (Kallinen et al., 2014; Keinanen et al., 2017), and ^{68}Ga (Tishchenko et al., 2020). In a previous work, PSi NPs were functionalized with bisphosphonate (BP), a robust and stable chelator for radiolabeling (Wen et al., 2022). BP-functionalized PSi (PSi-BP) NPs labeled with ^{99m}Tc and ^{68}Ga exhibited excellent radiochemical yield (>91 %) and radiochemical stability (>75 % within 24 h in phosphate buffer), providing proof of concept for PSi-BP NPs in nuclear imaging with other radioisotopes as well.

Plain NPs generally face the risk of being quickly eliminated by the mononuclear phagocytic system (MPS) *in vivo*, causing a short blood circulation time (Gustafson et al., 2015). One of the most widely exploited approaches to prolong blood circulation consists of using the hydrophilic polymer polyethylene glycol (PEG) for the surface coating of NPs (Shi et al., 2021). However, PEGylated nanoplatforms with non-specific ability can activate an anti-PEG immune response, leading to accelerated blood clearance after administration (Lila et al., 2013). Coating NPs with natural cell membranes, such as platelet membranes and cancer cell membranes (CCm), is a new approach for functionalizing different NPs with multiple biological benefits (Fang et al., 2022). For example, NPs coated with CCm possess the inherited surface membrane structure of cancer cells, endowing NPs with homotypic-targeting ability to tumors of the same kind (Ai et al., 2020). The most widely used methods for coating NPs with CCm are extrusion and sonication (Fang et al., 2023). For example, CT-26 cell membrane-coated porous silica NPs were recently developed in our group using the extrusion method. The resulting NPs presented a selective targeting ability to homotypic CT-26 cancer cells in competitive experiments with other cell lines such as MCF-7 and HeLa (Liu et al., 2021a). However, the most successful CCm coating was mainly achieved with NPs with regular shapes, such as spherical silica NPs (Cai et al., 2019), and the efficiency of CCm coating on NPs with irregular shapes remains barely explored. Moreover, the manual extrusion method may lead to high radiation exposure for the operator during NPs coating. Therefore, a simple and efficient method for coating irregular NPs (e.g., PSi) during the preparation of nuclear imaging agents is urgently needed.

Herein, we introduce a novel PEG-assisted membrane coating method by integrating chemical PEG grafting and physical CCm coating. First, BP molecules were conjugated on the surface of PSi NPs, which acted as the chelators for ^{89}Zr radiolabeling; Second, we used the PEG molecules to chemically functionalize the surface of ^{89}Zr-BP-PSi NPs to obtain PEG-^{89}Zr-BP-PSi NPs. Lastly, we designed an easy solvent-drying coating method to achieve a successful cancer cell membrane coating (Scheme 1). The radiolabeled, PEGylated, and biomimetic PSi NPs (CCm-PEG-^{89}Zr-BP-PSi NPs) showed relatively low cytotoxicity, good colloidal stability, and excellent radiochemical stability. The developed CCm-PEG-^{89}Zr-BP-PSi NPs exhibited efficient homotypic targeting abilities *in vitro* and *in vivo*. Overall, the present study demonstrated a novel approach for preparing biomimetic NPs with irregular shapes for targeted cancer imaging.

2. Materials and methods

2.1. Chemicals and materials

All chemicals and solvents were obtained from commercial providers, and they were used without further purification, including silicon wafers (Okmetic Oy), hydrofluoric acid (HF 38–40 %, Merck), ethanol (EtOH 99.5 %, Altia Oyj), hydrogen peroxide (H_2O_2, ACROS OrganicsTM), phosphate buffer (PBS, pH = 7.00 ± 0.02, VWR), fetal bovine serum (FBS, Sigma-Aldrich), mesitylene (99 %, ACROS OrganicsTM), hydrochloric acid (HCl, 37 %, Merck), methoxy-PEG-silane (PEG, 0.5 kDa, Gelest), methoxy-PEG-silane (PEG, 2 kDa, Biochempeg Scientific), 4′,6-diamidino-2-phenylindole (DAPI, Sigma-Aldrich), 1,1′-dioctadecyl-3,3,3′,3′-tetramethylindocarbocyanine perchlorate (DiI, Sigma-Aldrich), bicinchoninic acid (BCA) assay kit (Thermo Fisher Scientific), EDTA-free mini protease inhibitor tablet (Sigma-Aldrich), CellTiter-Glo assay kit (Promega), Cyanine 5.5 NHS ester (Cy5.5, Lumiprobe), 4-(2-hydroxyethyl)-1-piperazineethanesulfonic acid (HEPES, Biowest), Dulbecco's modified Eagle's medium (DMEM, VWR), Roswell Park Memorial Institute Medium (RPMI, VWR), and Hank's balanced salt solution (HBSS, HyClone). ^{89}Zr was bought from PerkinElmer. The synthesis of bisphosphonate has been described elsewhere (Riikonen et al., 2020).

2.2. Preparation of cancer cell membranes

The cancer cell membranes were collected following the ultracentrifugation method previously described by our group (Liu et al., 2021a). In brief, MAD-MB-231 cells were cultured in 150 mm plates with RPMI medium (10 % FBS and 1 % penicillin). At 80 % confluency, the cells were detached with 5 mL Trypsin-EDTA solution. After washing with HBSS (three times, 1200 × *g*/5 min), the cells were incubated in a hypotonic lysing buffer (20 mM Tris-HCl pH = 7.5, 10 mM KCl, 2 mM $MgCl_2$, and 1 EDTA-free mini protease inhibitor tablet per 10 mL of solution) at 4 ℃ for 30 min. The solution was disrupted under an ice bath with a Dounce homogenizer set to 100 passes and centrifuged at 3200 × *g*/5 min. The supernatant was collected, and another 5 mL hypotonic lysing buffer was added to re-disperse the pellet before repeating another 100 passes of homogenization followed by centrifugation. The supernatants were saved and spun down under 6000 × *g*/20 min. The pellet was discarded, and the supernatant was centrifuged at 4 ℃ under 100,000 × *g*/1h. The collected cancer cell membranes were washed once in 25 mM HEPES at 4 ℃ under 100,000 × *g*/0.5 h. The final pellet was collected and re-suspended in 25 mM HEPES after probe sonication under an ice bath for 1.5 min. The cell membrane proteins were quantified with a BCA assay kit, and the samples were stored at −20 ℃ for the subsequent experiments. The quantified CCm was stained with DiI (10 μg/mL) at 37 ℃ for 2 h, and then the excess dye was removed by washing with HEPES twice. DiI-labeled CCm was further used in homotypic targeting studies.

2.3. Synthesis of NPs

1) PSi NPs: The PSi films were obtained by electrochemical etching in a mixture (1:1HF (38–40 %)/ethanol) on silicon wafers (p+, 0.01–0.02 Ω cm). After drying at 65 °C/1h, the PSi films were milled in ethanol at 1000 rpm/1h with a planetary ball mill (Fritsch Pulverisette 7). Then particles with a size of around 160 nm were obtained by centrifuge and stored for subsequent use.
2) BP-PSi NPs: The NPs were obtained after the surface functionalization of the PSi NPs with the BP molecules. To remove the oxidized layer, 60 mL of 10.0 g/L PSi NPs were treated with HF (6 mL, 5 %) for 10 min. After being washed twice with ethanol and mesitylene, PSi NPs reacted with BP molecules via a hydrosilylation process at 120 °C under an N_2 atmosphere for 19 h in a quartz tube (1:2 mass ratio of BP to PSi NPs in mesitylene). The resulting BP-PSi NPs were washed twice with ethanol and dispersed in ethanol.
3) ^{89}Zr-BP-PSi NPs: ^{89}Zr-labelled NPs were synthesized by mixing the BP-PSi NPs with ^{89}Zr in HEPES buffer (pH 7.5) at 70 ℃ for 1 h (Bindini, 2021). To do this, 2 M sodium carbonate was used to neutralize the pH value of ^{89}Zr in oxalic acid (250 μL, 12.15 mCi, 401.5 MBq) to 7. The neutralized ^{89}Zr solution was added to the PSi-BP NPs solution (2 mg, 700 μL 25 mM HEPES buffer) and mixed well at 70 °C for 1 h. The NPs were centrifuged at 13,400 rpm/10 min, washed with water three times to remove free ^{89}Zr and re-dispersed in 1 mL ethanol. Radio-thin-layer chromatography was used to verify the radiochemical purity by spotting the NP suspension on a paper strip. The strips were eluted with ACN/citric acid (1/9, 20 mM) or EDTA (60 mM) and measured with a TLC reader (MiniGTA TLC, Raytest, Germany). The amount of radioactivity in the isolated NPs was measured using a dose calibrator (Capintec, USA).
4) Cy5.5 labeled NPs: NPs (50 mg in 10 mL ethanol) were first reacted with APTES (20 μL) for 2 h at room temperature. After being washed twice with ethanol, the aminated NPs (^{89}Zr-BP-PSi-NH_2 NPs) were reacted overnight with Cy5.5-NHS (0.25 mg in 1 mL ethanol) at room temperature. The excess amine groups were capped with succinic anhydride (10 mg in 2 mL of ethanol). The NPs were washed twice with ethanol to yield the ^{89}Zr-BP-PSi-Cy5.5-COOH NPs, which were further used for PEGylation and CCm coating.
5) PEG-^{89}Zr-BP-PSi NPs were synthesized following our previous work with a slight modification (Wen et al., 2022). PEG-silanes (100 μL 0.5 kDa and 50 mg of 2 kDa PEG-silane in 1 mL ethanol) were mixed with 1 mg ^{89}Zr-BP-PSi NPs; then the mixture was incubated at 90 °C/1h with airflow. The developed NPs were collected after washing twice with ethanol.
6) CCm-^{89}Zr-BP-PSi NPs were prepared using the solvent-drying method. A total of 0.5 mg ^{89}Zr-BP-PSi NPs and 0.5 mg CCm in 25 mM HEPES were mixed and then dried under airflow at room temperature to evaporate the solvent. CCm-PEG-^{89}Zr-PSi-BP NPs were prepared using the same method, except PEG-^{89}Zr-BP-PSi NPs were used. Cell membrane utilization was defined by the formula below:

$$P = \frac{C1 - C2}{C1} * 100\%$$

P is the effective utilization of cell membranes, *C1* is the initial concentration of cell membranes added during coating, and *C2* is the concentration of cell membranes in the supernatant after coating. The concentration of the cell membranes was quantified by a BCA kit.

2.4. Physicochemical characterization

The morphology of the NPs was measured with transmission electron microscopy (TEM, JEOL JEM2100F) after drying a droplet of the NPs suspension onto a copper grid. The zeta potential of the NPs was measured in deionized water at room temperature, and the hydrodynamic size of all NPs was measured in buffer solutions at 37 °C (Zetasizer Nano ZS, Malvern Instruments). The BP content of the NPs was determined with thermogravimetry analysis (TGA Q50, TA instruments) under N_2 flow (200 mL/min) with the steps of equilibration at 80 °C/30 min and then heating to 800 °C at a rate of 20 °C/min. The CCm coating was verified with Fourier-transform infrared spectroscopy (FTIR, Nicolet 8700, Thermo Scientific) and sodium dodecyl sulfate polyacrylamide gel electrophoresis (SDS-PAGE). Scanning electron microscopy (SEM, Zeiss Sigma HP VD) with energy-dispersive X-ray spectrometer (EDS) was used to analyze the elements of NPs to verify the successful BP conjunction and PEGylation. The samples were prepared after drying a droplet of the NPs suspension onto aluminum specimen stubs. The elemental analysis was done at 5 kV with Thermo Pathfinder software.

The colloidal stability of NPs was evaluated after the total decay by incubating NPs with PBS and cell medium at 37 °C for 24 h. At various time intervals, the size distribution of NPs was measured by Zetasizer. In addition, the CCm content on the surface of NPs before and after the incubation in PBS for 24 h was quantified by a BCA kit. The radiochemical stability of NPs was evaluated by incubating NPs with PBS and cell medium at 37 °C up to 48 h. At different time points, the NPs were separated by centrifugation, and the amounts of radioactivity in the pellet and the supernatant were quantified. The radiochemical stability of NPs was calculated as the ratio between the amount of radioactivity in the pellet and the total amount of radioactivity (pellet + supernatant).

2.5. Cell cytotoxicity

The cytotoxicities of the PSi, BP-PSi, ^{89}Zr-BP-PSi, PEG-^{89}Zr-BP-PSi, and CCm-PEG-^{89}Zr-BP-PSi NPs were examined using a CellTiter-Glo Luminescent Cell Viability Assay kit. MDA-MD-231 cells were seeded in a 96-well plate at a density of 1×10^4 cells/well and cultured for 24 h in 100 μL DMEM supplemented with 10 % FBS and 1 % penicillin–streptomycin. The medium was changed to 100 μL of fresh medium containing various concentrations of PSi, BP-PSi, ^{89}Zr-BP-PSi, PEG-^{89}Zr-BP-PSi, and CCm-PEG-^{89}Zr-BP-PSi NPs. The cell medium was used as the negative control. After 24 h incubation at 37 °C, the cell viability was quantified using the CellTiter Glo assay in a Synergy H1 microplate reader (Biotek, Winooski, USA). All samples had five replicates (Li et al., 2020).

2.6. Homotypic targeting studies

To verify our hypothesis that CCm-coated NPs can be well self-recognized by homotypic cancer cells, MDA-MB-231, Raw 267.4, MCF-7, Hela, and mouse embryonic fibroblast cell lines were seeded in 8-well plates (2.5×10^4 cells/well) for 24 h in 200 μL cell medium. The medium was changed to a medium containing 50 μg/mL NPs (experimental group: CCm-PEG-^{89}Zr-BP-PSi NPs, control groups: ^{89}Zr-BP-PSi, PEG-^{89}Zr-BP-PSi, and CCm-^{89}Zr-BP-PSi). After 4 h incubation, the cells were washed with HBSS three times, fixed with 4 % paraformaldehyde solution for 10 min, and washed with HBSS twice before the last incubation in DAPI solution (10 μg/mL in 200 μL HBSS) for 10 min at room temperature. The internalization of NPs was measured with a confocal laser scanning microscope (CLSM, Zeiss LSM 700, Carl Zeiss, Jena, Germany), where the PSi NPs, CCm, and cell nuclei were marked with Cy5.5 (red), DiI (orange) and DAPI (blue), respectively. The mean fluorescence intensity (MFI) of images was quantified by Zeiss Zen Blue imaging analysis software. TEM (JEOL JEM2100F) was used to confirm the cell internalization of the different NPs. To this end, 2×10^5 cells/well different cell lines were seeded in a 24-well plate. After 24 h of culture, the cells were washed once with HBSS and then incubated with a medium containing 50 μg/mL NPs for 4 h. Subsequently, the cells were fixed with 2 % glutaraldehyde and 0.1 M phosphate buffer at 37 °C for 1 h, washed twice with 0.1 M phosphate buffer for 5 min, postfixed with 1 % osmium tetroxide in 0.1 M phosphate buffer for 1 h and washed twice with 0.1 M phosphate buffer for 5 min. The samples were cut to obtain 60–80 nm frontal sections and stained with uranyl acetate after dehydrated and embedded in epoxy resin.

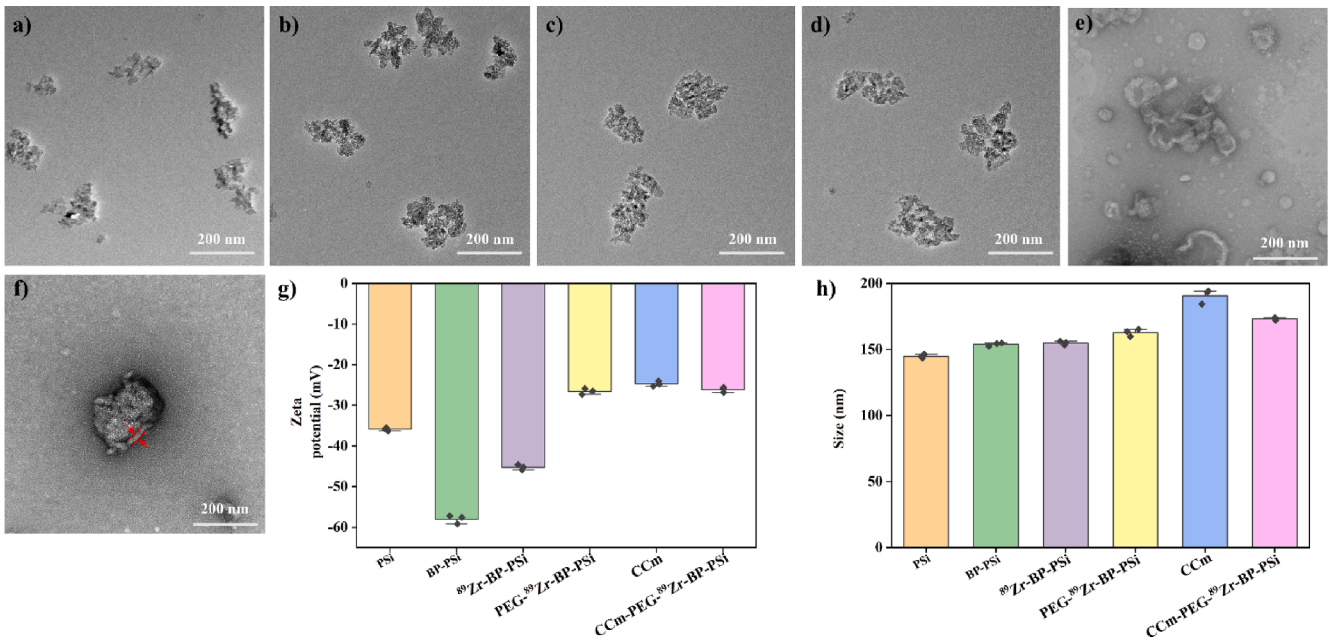

Fig. 1. Transmission electron microscopy (TEM) images: a) PSi, b) BP-PSi, c) ^{89}Zr-BP-PSi, d) PEG-^{89}Zr-BP-PSi, e) CCm after negative staining, f) CCm-PEG-^{89}Zr-BP-PSi after negative staining (red arrow points out CCm coating), g) mean diameter and h) zeta potential of all types of NPs and pure MDA-MB-231 CCm. Data represent mean ± SD (n = 3).

2.7. PET/CT imaging in vivo

Animals were maintained and handled following institutional, national, and EU regulations and guidelines. Animals were all anesthetized with a mixture (3–5 % isoflurane in O_2) to achieve induction before each procedure, while the mixture was reduced to 1.5–3 % prior to intravenous administration. Eight-week-old female Swiss nude mice (Charles River Laboratories, France) were subcutaneously injected with 100 μL cold PBS: Matrigel (1:1) containing 4×10^6 MDA-MB-231 cells into the back of each mouse. Three weeks after the injection, the tumor-bearing mice were used for further experiments.

Intravenous injections (100 μL, 4 % mannitol, 1 mg/mL) were carried out through the tail vein of the MDA-MB-231 tumor-bearing mice (3 mice/per group: PEG-^{89}Zr-BP-PSi, and CCm-PEG-^{89}Zr-BP-PSi NPs). The injected sample had an activity of 80–170 μCi (2.96–6.29 MBq). Static PET images (5 min duration) were acquired at t = 1, 4, 24, and 48 h post administration, using a β-Cube scanner (Molecubes, Belgium). After each PET acquisition, the animals were subjected to a CT scan using a γ-Cube scanner (Molecubes, Belgium) for anatomical reference and to generate an attenuation map for PET image reconstruction. PET images were reconstructed using a 3D OSEM reconstruction algorithm and applying random, scatter, and attenuation corrections. PET and CT images of the same mouse were co-registered and analyzed using the PMOD image processing tool (PMOD Technologies LLC, Switzerland; version 3.4). Volumes of interest (VOIs) were manually delineated in major organs, and activity values (decay-corrected) were obtained as kBq/cm^3. The values were then corrected by applying a calibration factor obtained from previous scans on a phantom (micro-deluxe, Data Spectrum Corp.) under the same experimental conditions (isotope, reconstruction, algorithm, and energy window).

2.8. Biodistribution in vivo

All animals were sacrificed 48 h post-injection (p.i.), and the main organs and tumors were harvested and weighed. The amount of radioactivity in each organ was measured using a gamma counter (Wallach Wizard, PerkinElmer, Waltham, MA, USA). The %ID g^{-1} (percent injected dose per gram of tissue) was calculated by normalizing toward the total radioactivity injected (decay-corrected) and organ weights.

2.9. Statistical analysis

Statistically significant differences were tested with an unpaired two-tailed Student *t*-test (Microsoft, Excel). Data were reported as mean ± standard deviation. $p < 0.05$ were considered significant. * indicates $p < 0.05$, ** indicates $p < 0.01$, and *** indicates $p < 0.001$.

3. Results and discussion

3.1. Preparation of biomimetic NPs

Prior to PEGylation, attempts were made to coat the ^{89}Zr-BP-PSi NPs directly through extrusion and sonication methods following previously published works.(Guo et al., 2022; Rahikkala et al., 2020) However, the colloidal stability of the resulting NPs was poor, as shown in Fig. S1. In the extrusion method, the initial resuspension of the NPs in a PBS solution resulted in an immediate size increase of ~80 nm, followed by a further increase of ~160 nm after 24 h incubation. Furthermore, the yield was meager, as a significant portion of the NPs were blocked at the polycarbonate membrane during the process. The sonication method also significantly increased the size of the NPs, reaching 450 nm after incubation in PBS for 24 h. These results demonstrate that both methods failed to coat ^{89}Zr-BP-PSi NPs directly with CCm. Consequently, PEGylation of the NPs before solvent-drying CCm coating was explored to improve their stability. The effects of reaction temperature and PEG amount were investigated (Fig. S2). PEGyaltion with two different weight PEG molecules (2 kDa and 0.5 kDa) was used to obtain the PEG-^{89}Zr-BP-PSi NPs under optimized conditions (1 mg NPs + 50 mg 2 k PEG + 100 μL 0.5 k PEG in 90 ℃/1h). The PEGylation facilitated successful CCm coating of PEG-^{89}Zr-BP-PSi NPs via the solvent-drying method, leading to well-dispersed and stable CCm-PEG-^{89}Zr-BP-PSi NPs, as discussed in the next sections.

3.2. Physiochemical characterization

The synthetic route of NPs is shown in Scheme 1. PSi NPs were

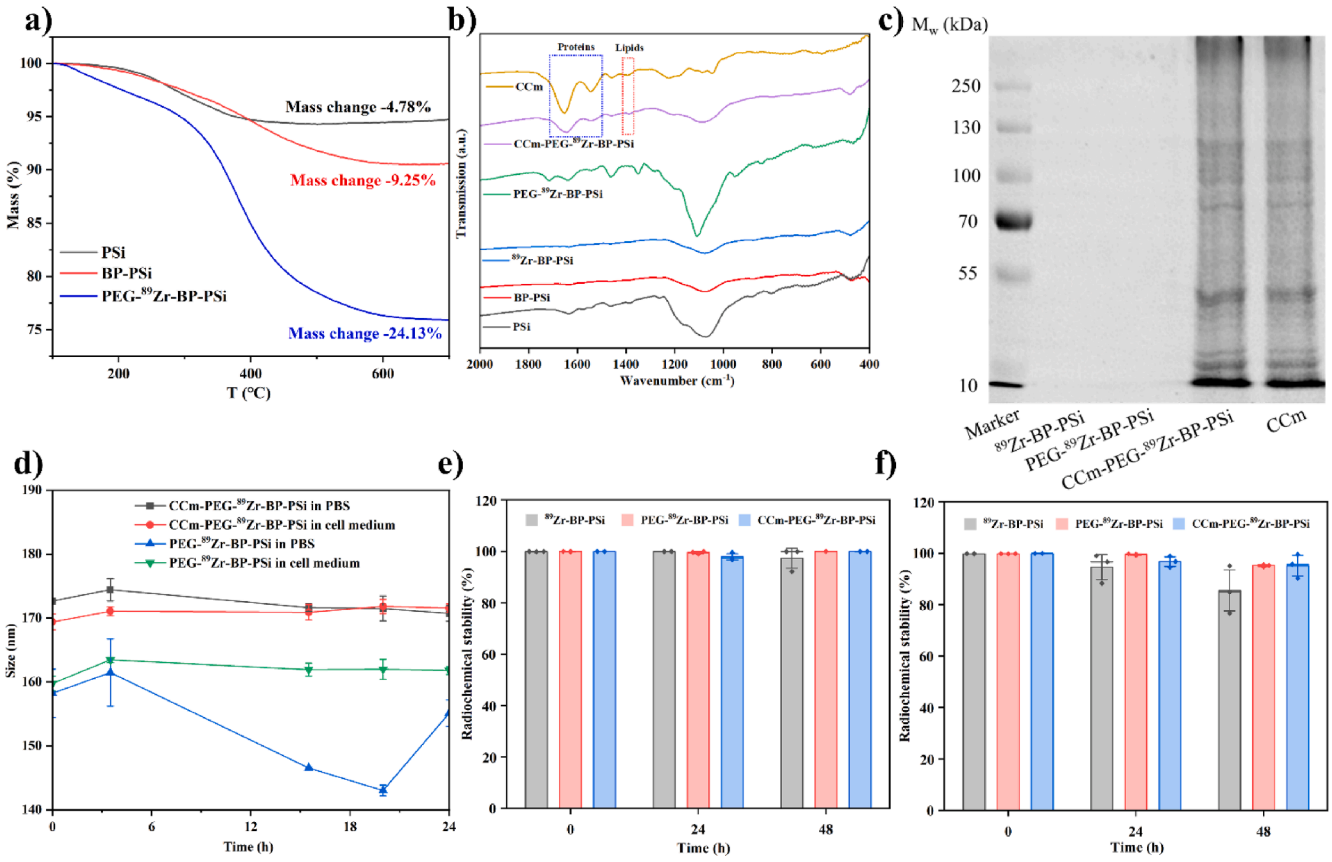

Fig. 2. Physicochemical characterizations of different NPs: a) thermogravimetric analysis (TGA) curves, b) Fourier transform infrared spectroscopy (FTIR) spectra, c) SDS-PAGE protein analysis (Coomassie staining), d) colloidal stability in PBS and cell medium at 37 ℃ for 24 h. Radiochemical stability in e) cell medium and f) PBS at 37 ℃ for 0, 24, and 48 h. Data represent mean ± SD (n = 3).

produced by ball-milling films prepared with electrochemical etching of silicon wafers. BP-PSi NPs were synthesized by following the procedure in our previous work, in which BP molecules were conjugated with the Si-H groups on the surface of PSi NPs by hydrosilylation (Wen et al., 2022). The chelator-assisted radiolabeling procedure depends on the solid affinity between BP molecules (phosphate groups) and Zr^{4+} ions under the HEPES buffer solution (pH ~7) at 70 ℃ for 1 h. The shapes of the NPs were examined using TEM measurements (Fig. 1a–f). Similar to PSi, the NPs of BP-PSi, ^{89}Zr-BP-PSi, and PEG-^{89}Zr-BP-PSi were monodisperse and irregular without any shape changes after BP loading, ^{89}Zr radiolabeling, or PEGylation, respectively. However, a clear external layer was observed on the CCm-PEG-^{89}Zr-BP-PSi NPs because of the CCm coating (Fig. 1f and Fig. S3). Compared to ^{89}Zr-BP-PSi (155 ± 2 nm), a gradual increase in hydrodynamic diameter was observed after PEGylation and CCm coating: 163 ± 3 nm (PEG-^{89}Zr-BP-PSi), and 173 ± 1 nm (CCm-PEG-^{89}Zr-BP-PSi) (Fig. 1g). Furthermore, the zeta potentials of PSi, BP-PSi, ^{89}Zr-BP-PSi, PEG-^{89}Zr-BP-PSi, pure CCm, and CCm-PEG-^{89}Zr-BP-PSi were −35.0 ± 0.4, −58 ± 1, −45 ± 1, −26.6 ± 0.7, −24.7 ± 0.7, and −26.1 ± 0.6 mV, respectively (Fig. 1h). The BP-PSi NPs were more negative than the PSi NPs due to the phosphate groups from the BP molecules. Further, successful ^{89}Zr radiolabeling and PEGylation led to the lower negativity of the as-formed NPs.

TGA was used to quantify the amount of BP grafted on PSi NPs, which was ~4.47 wt%, equivalent to 139 μmol BP (MW = 330 g/mol) per gram of sample. The PEG amount was ~14.88 wt%, validating the success of PEGylation (Fig. 2a). EDS mapping and spectrum analysis demonstrated that the decreasing density of element Si and increasing density of element C and P, further verifying the successful BP conjunction and PEGyaltion (Fig. 4S). During the membrane coating, we also investigated the effect of the weight ratios of CCm/ NPs (0.5, 1, 2) on the effective utilization of the cell membrane (Fig. S5). Notably, we observed that effective membrane utilization reached the highest value when a ratio of 1 was used (26.0 ± 0.6 %, compared to 4 ± 2 % and 20.6 ± 0.3 % for ratios of 0.5 and 2, respectively). The results indicated a threshold (26.0 ± 0.6 %) above which the membranes could not be further coated on the surface. FTIR spectra presented typical peaks of the protein (1500–1700 cm^{-1}) and lipid (1400–1450 cm^{-1}) absorption bands from pure CCm and CCm-PEG-^{89}Zr-BP-PSi NPs, further indicating a successful membrane coating (Fig. 2b) (Bangaoil et al., 2020). Additionally, the membrane reservation on CCm-PEG-^{89}Zr-BP-PSi NPs was confirmed by SDS-PAGE. The CCm-PEG-^{89}Zr-BP-PSi NPs retained almost all membrane proteins compared to the original CCm (Fig. 2c). Due to the PEGylation, and CCm coating, PEG-^{89}Zr-BP-PSi and CCm-PEG-^{89}Zr-BP-PSi NPs were both stable in PBS or a cell medium solution at 37 ℃ for 24 h (Fig. 2d). After the 24 incubation in PBS, there were 76 ± 5 % remaining CCm, equal to ~0.2 mg of CCm per 1 mg of NPs on the surface (Table S1). As a control group, the CCm-^{89}Zr-BP-PSi NPs were synthesized directly by CCm coating without PEGylation. The size of CCm-^{89}Zr-BP-PSi NPs was 299 ± 5 nm higher than 77 ± 5 nm (CCm-PEG-^{89}Zr-BP-PSi), highlighting the critical role of the PEG molecules in preventing aggregation during the CCm coating procedure. The colloidal stability test revealed that CCm-^{89}Zr-BP-PSi NPs had around a 100 nm size increase after incubating in PBS and cell medium at 37 ℃ for 24 h, further verifying that PEGylation assisted the CCm coating (Fig. S6a). Additionally, the zeta potential of CCm-^{89}Zr-BP-PSi NPs without PEGylation was −30.4 ± 0.8 mV (Fig. S6b), which was more negative than CCm-PEG-^{89}Zr-BP-PSi (−26.1 ± 0.6 mV). The typical TEM of CCm-^{89}Zr-BP-PSi was shown in Fig. S6c. The radiochemical yields of ^{89}Zr-BP-PSi, PEG-^{89}Zr-BP-PSi, and CCm-PEG-^{89}Zr-BP-PSi NPs were all above 95 % (Fig. S7). Based on the radio-TLC results, radiochemical purity values

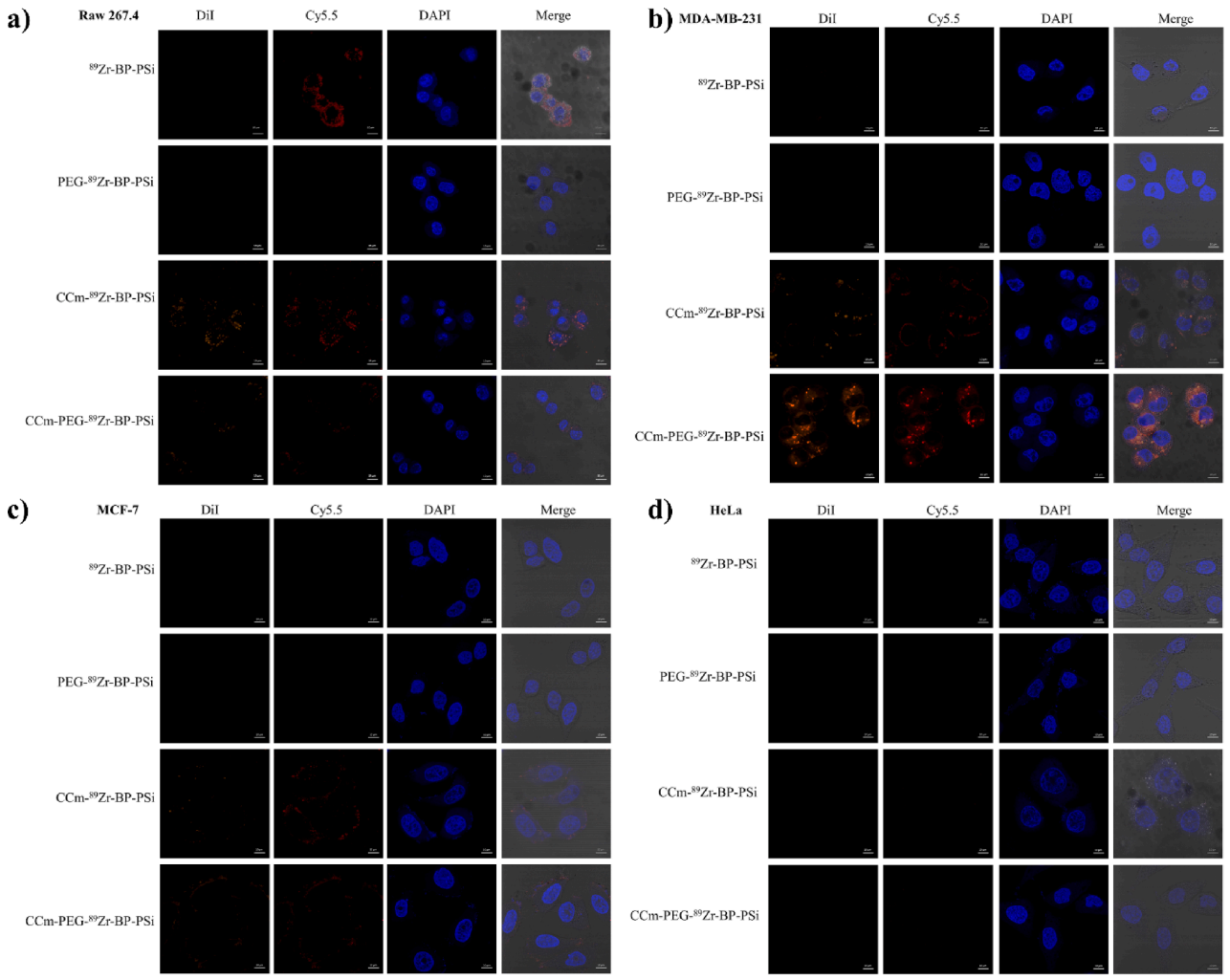

Fig. 3. Representative confocal laser scanning microscopy (CLSM) images of cells after 4 h incubation with 50 μg/mL ^{89}Zr-BP-PSi, PEG-^{89}Zr-BP-PSi, CCm-^{89}Zr-BP-PSi, and CCm-PEG-^{89}Zr-BP-PSi NPs: a) Raw 267.4, b) MDA-MB-231, c) MCF-7, and d) HeLa. The PSi cores and cancer cell membranes (CCm) were labeled with Cy5.5 (red) and DiI (orange), respectively. Cell nuclei were stained with DAPI (blue): scale bars, 10 μm.

were ~99 % (Fig. S8). The radiochemical stability of NPs was examined *in vitro* by incubating them in PBS and cell medium for 48 h (Fig. 2e-f). In PBS, both PEG-^{89}Zr-BP-PSi and CCm-PEG-^{89}Zr-BP-PSi had a slight Zr release (~4.8 %). A higher release was observed for ^{89}Zr-BP-PSi (~15.5 %) after 48 h because of the protection from the PEG layer and CCm layer. However, all the nanoparticles had good radiochemical stability in the cell medium after 48 h of incubation. One possible explanation is that the higher hydrolysis rate of NPs in PBS than in the cell medium led to a difference in radiochemical stability.

3.3. *In vitro cytotoxicity and homotypic targeting experiments*

The samples were incubated with the MDA-MB-231 cell line to evaluate their biocompatibility. With an increase in the concentration of NPs, the non-PEGylated and non-CCm coated NPs (PSi, BP-PSi, and ^{89}Zr-BP-PSi) showed significant concentration-dependent toxicity. However, PEG-^{89}Zr-BP-PSi and CCm-PEG-^{89}Zr-BP-PSi NPs presented negligible cytotoxicity when the concentration was up to 250 μg/mL (Fig. S9), in line with our previous work related to PEGylated and membrane-coated NPs (Liu et al., 2022; Näkki et al., 2015). NPs were labeled with Cy5.5 to enable the study of homotypic targeting ability with fluorescence microscopy. The physicochemical characterizations of the dye-labeled NPs, including FTIR, TGA, size distribution, and zeta potential, indicated successful conjugation of the dye on the NPs (Fig. S10) (Tamarov et al., 2021). Next, CCm-PEG-^{89}Zr-BP-PSi NPs, as well as control groups (^{89}Zr-BP-PSi, CCm-^{89}Zr-BP-PSi, and PEG-^{89}Zr-BP-PSi NPs), were incubated with four cell lines (RAW 267.4, MDA-MB-231, MCF-7, and HeLa), after marking the CCm, PSi core, and cell nuclei with DiI (orange), Cy5.5 (red), and DAPI (blue), respectively. With the RAW 267.4 cell line, the group treated with ^{89}Zr-BP-PSi NPs showed the strongest fluorescence because of the plain NPs without stealth properties, causing enhanced macrophage cell uptake. CCm-^{89}Zr-BP-PSi NPs also had robust fluorescence, indicating that the direct coating method failed and could not improve the immune escape ability of the NPs. Both PEG-^{89}Zr-BP-PSi and CCm-PEG-^{89}Zr-BP-PSi showed nearly no uptake evidencing successful PEGylation and PEG-assisted CCm coating (Fig. 3a). After incubation with CCm-PEG-^{89}Zr-BP-PSi NPs, MDA-MB-231 cells showed the highest intensity of orange and red fluorescence compared to the control groups, confirming homotypic targeting of the CCm-coated NPs (Fig. 3b). Similar weak signals were observed in the MCF-7 cell line treated with CCm-^{89}Zr-BP-PSi and CCm-PEG-^{89}Zr-BP-PSi. One explanation is that cell membranes from MDA-MB-231 and MCF-7 have similar compositions (Fig. 3c) (He et al., 2015). However, with the HeLa cell line, all the groups had negligible fluorescence signals (Fig. 3d); similar signals were also observed in the mouse embryonic fibroblast cell line (Fig. S11a). The quantitative results based on the CLSM images revealed that the MDA-MB-231 cell incubated with CCm-PEG-^{89}Zr-BP-PSi NPs had the strongest MFI than those of ^{89}Zr-BP-PSi, PEG-^{89}Zr-BP-PSi and

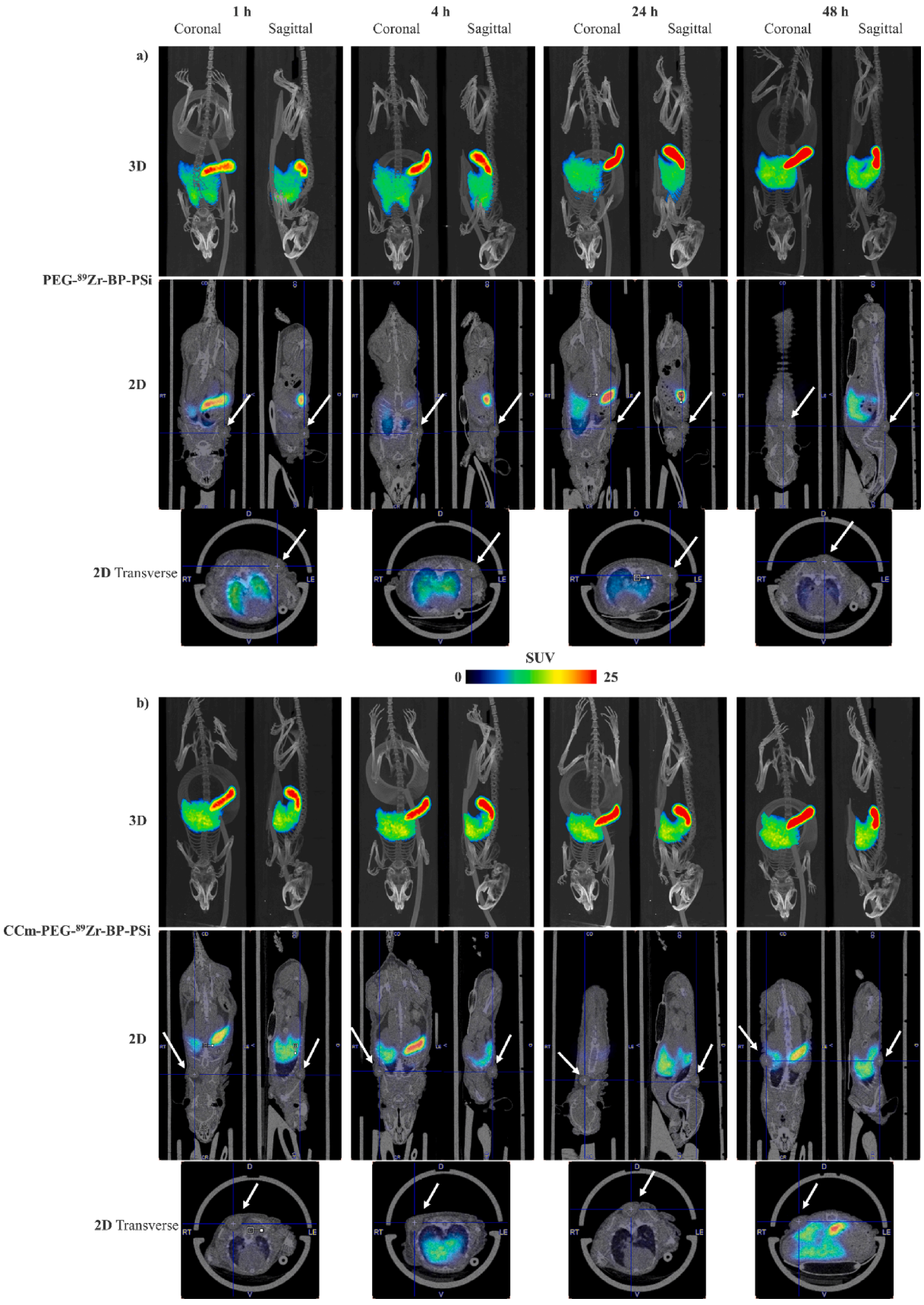

Fig. 4. Representative 3D and selected 2D PET/CT images of a) PEG-^{89}Zr-BP-PSi, and b) CCm-PEG-^{89}Zr-BP-PSi NPs measured 1, 4, 24, and 48 h post-injection in the tail vein of MDA-MB-231 tumor-bearing mice. Arrows indicate the tumor areas.

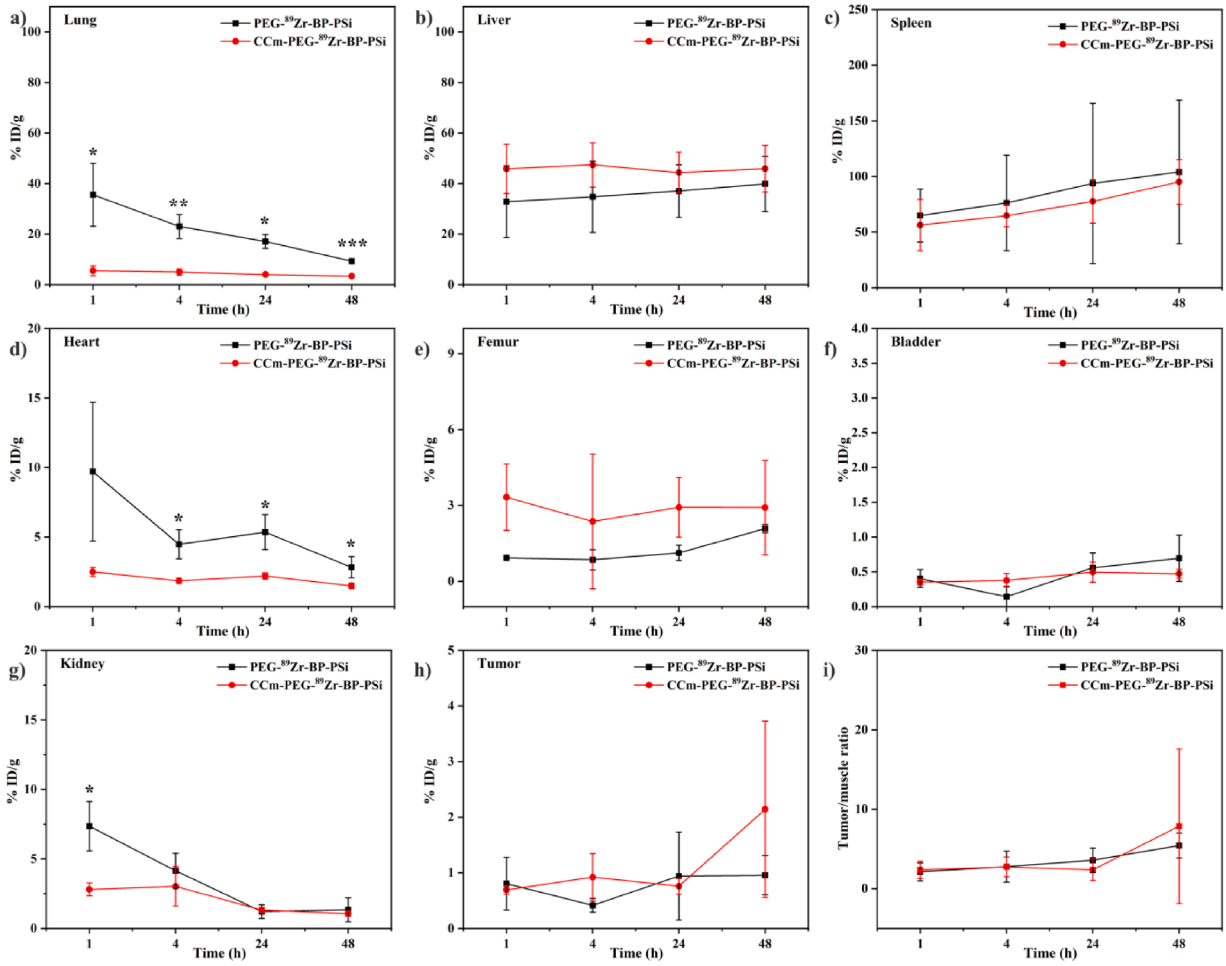

Fig. 5. The concentration of radioactivity in different organs obtained from quantification of PET images, expressed as a percentage of injected dose per gram of tissue: a) lungs, b) liver, c) spleen, d) heart, e) femur, f) bladder, g) kidney, and h) tumor; i) tumor to muscle ratio measured 1, 4, 24, and 48 h after tail vein injection in MDA-MB-231 tumor-bearing mice. Data represent mean ± SD (n = 3). * indicates $p < 0.05$, ** indicates $p < 0.01$, and *** indicates $p < 0.001$.

CCm-^{89}Zr-BP-PSi NPs. Moreover, CCm-PEG-^{89}Zr-BP-PSi NPs did not have an affinity advantage for other cell lines, indicating the homotypic ability of CCm-PEG-^{89}Zr-BP-PSi NPs to homologous MDA-MB-231 cell (Fig. S11b-c). We also used TEM to confirm the homotypic targeting property of CCm-PEG-^{89}Zr-BP-PSi NPs; the results were consistent with the CLSM images. Specifically, both CCm-^{89}Zr-BP-PSi NPs and ^{89}Zr-BP-PSi had enhanced intracellular uptake by RAW 267.4 cells. A large number of CCm-PEG-^{89}Zr-BP-PSi NPs were also located inside the endocytic vesicles of MDA-MB-231 cell lines but were rarely found in other cell lines. Moreover, few NPs were found inside MCF-7 and HeLa cells (Fig. S12).

3.4. *In vivo* imaging study

Encouraged by the efficient homotypic targeting ability *in vitro*, we explored the *in vivo* targeting performance of the biomimetic PSi as PET/CT imaging agents with MDA-MB-231 tumor-bearing mice. After the intravenous injection of radiolabeled NPs, static PET imaging was carried out at different time points (1, 4, 24, and 48 h p.i.) (Fig. 4). The 3D coronal and sagittal PET/CT images clearly indicated that a small part of PEG-^{89}Zr-BP-PSi NPs accumulated in the lung at 1 h (p.i.) and then decreased with time. However, increased uptake was observed in the liver and spleen after administration. CCm- PEG-^{89}Zr-BP-PSi NPs showed a rapid accumulation in the liver and spleen after the administration. Compared with the MPS organs (liver, spleen, and lungs), the relatively low amount of radioactivity in the tumors could not be visualized in the 3D PET/CT images or selected 2D PET/CT images. This might be due to different causes. One of which could be the rapid sequestration of the NPs by MPS organs, which decreased bioavailability, thus compromising tumor uptake. Most importantly, the small size of the tumors when images were acquired could be a reason for the lack of abundant vasculature (Table S2), leading to poor performance in the enhanced permeation and retention effect, which is an essential factor in determining the efficacy of active targeting (such as homotypic targeting) *in vivo* (Sun et al., 2022).

Based on the CT images, volumes of interest (VOIs) were drawn from different organs to obtain quantitative data. The concentration of radioactivity in each VOI was expressed as a percentage of the injected dose per gram of organ/tissue (%ID/g) (Fig. 5). The accumulation of PEG-^{89}Zr-BP-PSi and CCm-PEG-^{89}Zr-BP-PSi NPs in the lungs was 37 ± 11 %ID/g (1 h p.i.) and 6 ± 2 %ID/g (1 h p.i.), respectively (Fig. 5a). The remarkable accumulation difference may result from the decreased interaction between NPs and pulmonary surfactants in the lungs after CCm coating (Beck-Broichsitter and Bohr, 2019; Liu et al., 2021b). Obviously, most PEG-^{89}Zr-BP-PSi and CCm-PEG-^{89}Zr-BP-PSi NPs were initially located in the liver and spleen, with a typical accumulation pattern (Fig. 5b-c) very similar to those of previous works (Lumen et al., 2019; Lumen et al., 2021; Wen et al., 2022). One possible explanation is that both PEG-^{89}Zr-BP-PSi (−26.6 ± 0.7 mV) and CCm-PEG-^{89}Zr-BP-PSi NPs (−26.1 ± 0.6 mV) were negatively charged, increasing the interactions with macrophages in the liver and spleen (An et al., 2019). The radioactivity concentration of PEG-^{89}Zr-BP-PSi and CCm-PEG-^{89}Zr-

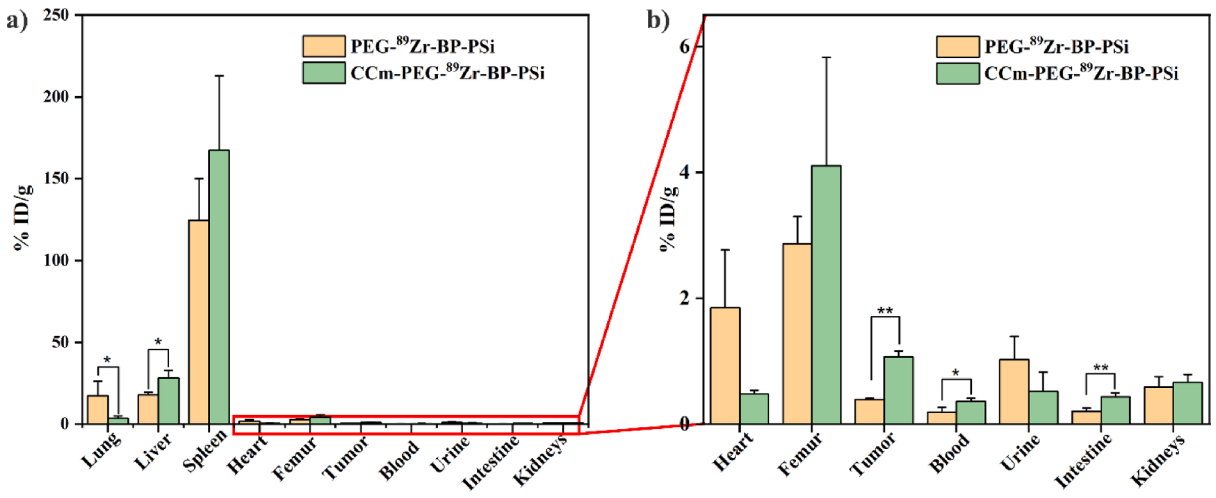

Fig. 6. *Ex vivo* biodistribution of NPs in selected organs at 48 h. Data represent mean ± SD (n = 3). * indicates $p < 0.05$, and ** indicates $p < 0.01$.

BP-PSi NPs in the liver and spleen slightly increased over time. In the heart, both NPs followed a similar declining trend. (Fig. 5d) During the imaging process, a small part of the free ^{89}Zr was released because of the biodegradation of the PSi NPs. Thus, a minor amount of radioactivity could be found in the kidneys, bladder, and femur (Fig. 5e-g). Most importantly, CCm-PEG-^{89}Zr-BP-PSi NPs had a 2-fold tumor accumulation of 2.1 ± 1.6 %ID/g (48 h p.i.) compared to PEG-^{89}Zr-BP-PSi (0.9 ± 0.4 %ID/g) after 48 h of blood circulation (Fig. 5h). The tumor/muscle ratios of both NPs were higher than 1 at the beginning of the experiments and gradually increased with time, reaching a maximum value of 5 ± 1 (PEG-^{89}Zr-BP-PSi, 48 h p.i.) and 8 ± 9 (CCm-PEG-^{89}Zr-BP-PSi, 48 h p.i.) after administration (Fig. 5i). These results evidenced the benefit of homotypic targeting by CCm coating of the NPs.

After 48 h post-injection, the *ex vivo* biodistribution demonstrated that most NPs accumulated in MPS organs (liver, spleen, and lungs) (Fig. 6), strongly agreeing with the visualized PET/CT imaging results and the VOI quantification analysis (Figs. 4 and 5). Compared to the minor accumulation in the kidney, high MPS organ uptake confirmed that hepatobiliary system clearance was apparently the main excretion route for both NPs (Karageorgou et al., 2022; Wang et al., 2021). The tumor radioactivity of CCm-PEG-^{89}Zr-BP-PSi NPs was 1.1 ± 0.1 %ID/g (48 h p.i.), significantly higher than that of PEG-^{89}Zr-BP-PSi NPs (0.4 ± 0.1 %ID/g, 48 h p.i.). By contrast, the %ID/g of CCm-PEG-^{89}Zr-BP-PSi NPs in blood was 0.36 ± 0.05 %ID/g (48 h p.i.), which was 90 % higher than that of PEG-^{89}Zr-BP-PSi NPs (0.19 ± 0.08 %ID/g, 48 h p.i.). Overall, the presence of CCm coating on the surfaces of CCm-PEG-^{89}Zr-BP-PSi NPs could efficiently enhance tumor-targeting uptake with a long blood circulation time.

4. Conclusion

In this work, we efficiently designed novel PEGylated and CCm-coated PSi NPs. By integrating BP molecules to serve as the chelator for ^{89}Zr, the as-synthesized nanoplatforms (CCm-PEG-^{89}Zr-BP-PSi NPs) displayed good colloidal stability, radiochemical stability, cytocompatibility, and targeting ability *in vitro*. PET/CT images and *ex vivo* biodistribution analysis showed the accumulation of NPs primarily in MPS organs. Nonetheless, CCm-PEG-^{89}Zr-BP-PSi NPs had relatively higher blood retention and tumor accumulation after 48 h post-injection than the control group's performance (PEG-^{89}Zr-BP-PSi NPs), highlighting the importance of CCm in enhancing the blood circulation and tumor targeting abilities of NPs. The *in vivo* active targeting performance of the NPs was probably limited by the presence of small-sized tumors with low-density blood vessels, reducing the enhanced permeation and retention effect, which is the basis of active targeting. Overall, these preliminary results indicate that the developed biomimetic NPs have the potential as targeting imaging agents for TNBC. We anticipate that with further modifications, such as drug loading, these biomimetic PSi NPs could be employed for targeted chemotherapy in treating TNBC.

CRediT authorship contribution statement

Huang Wen: Conceptualization, Data curation, Formal analysis, Investigation, Methodology, Validation, Writing – original draft. **María Gómez Martínez:** Investigation, Methodology, Resources, Writing – review & editing. **Emilia Happonen:** Investigation, Methodology, Resources, Writing – review & editing. **Jing Qian:** Investigation, Methodology, Resources, Writing – review & editing. **Vanessa Gómez Vallejo:** Investigation, Methodology, Resources. **Helena Jorge Mendazona:** Investigation, Methodology, Resources, Writing – review & editing. **Kimmo Jokivarsi:** Investigation, Methodology, Resources, Writing – review & editing. **Mauro Scaravilli:** Investigation, Methodology, Resources. **Leena Latonen:** Investigation, Methodology, Resources, Writing – review & editing. **Jordi Llop:** Conceptualization, Funding acquisition, Supervision, Writing – review & editing, Supervision, Project administration, Funding acquisition. **Vesa-Pekka Lehto:** Conceptualization, Funding acquisition, Project administration, Supervision, Writing – review & editing. **Wujun Xu:** Conceptualization, Funding acquisition, Project administration, Supervision, Writing – review & editing.

Declaration of competing interest

The authors declare that they have no known competing financial interests or personal relationships that could have appeared to influence the work reported in this paper.

Data availability

Data will be made available on request.

Acknowledgments

We thank Okmetic for the donation of the silicon wafers. We thank Jari Leskinen and Virpi Miettinen at SIB Labs of the University of Eastern Finland for their technical support in TEM imaging. We thank Tapio Nevalainen at School of Pharmacy of the University of Eastern Finland for supporting *in vitro* experiments. This work was supported by the Academy of Finland (project 314412) and the University of Eastern Finland's Doctoral Programme in Science, Technology, and Computing

(project 29980041). JL thanks Grant PID2020-117656RB-I00 funded by MCIN/AEI/ 10.13039/501100011033. Part of the *in vivo* work was carried out at the ReDIB ICTS infrastructure at CIC biomaGUNE, Ministry for Science and Innovation (MCIN).

Appendix A. Supplementary data

Supplementary data to this article can be found online at https://doi.org/10.1016/j.ijpharm.2023.123764.

References

Ai, X., Wang, S., Duan, Y., Zhang, Q., Chen, M.S., Gao, W., Zhang, L., 2020. Emerging approaches to functionalizing cell membrane-coated nanoparticles. Biochemistry 60 (13), 941–955.

An, L., Wang, Y., Lin, J., Tian, Q., Xie, Y., Hu, J., Yang, S., 2019. Macrophages-mediated delivery of small gold nanorods for tumor hypoxia photoacoustic imaging and enhanced photothermal therapy. ACS Appl. Mater. Interfaces 11 (17), 15251–15261.

Bangaoil, R., Santillan, A., Angeles, L.M., Abanilla, L., Lim Jr, A., Ramos, M.C., Fellizar, A., Guevarra Jr, L., Albano, P.M., 2020. ATR-FTIR spectroscopy as adjunct method to the microscopic examination of hematoxylin and eosin-stained tissues in diagnosing lung cancer. PLoS One 15 (5), e0233626.

Beck-Broichsitter, M., Bohr, A., 2019. Bioinspired polymer nanoparticles omit biophysical interactions with natural lung surfactant. Nanotoxicology 13 (7), 964–976.

Bindini, E., Ramirez, M.d.l.A., Rios, X., Cossío, U., Simó, C., Gomez-Vallejo, V., Soler-Illia, G., Llop, J., Moya, S.E., 2021. In vivo tracking of the degradation of mesoporous silica through ^{89}Zr radio-labeled core–shell nanoparticles. Small 2101519.

Cai, D., Liu, L., Han, C., Ma, X., Qian, J., Zhou, J., Zhu, W., 2019. Cancer cell membrane-coated mesoporous silica loaded with superparamagnetic ferroferric oxide and Paclitaxel for the combination of Chemo/Magnetocaloric therapy on MDA-MB-231 cells. Sci. Rep. 9 (1), 14475.

Chudgar, A.V., Mankoff, D.A., 2017. Molecular imaging and precision medicine in breast cancer. PET Clinics 12 (1), 39–51.

Fang, R.H., Gao, W., Zhang, L., 2022. Targeting drugs to tumors using cell membrane-coated nanoparticles. Nat. Rev. Clin. Oncol. 1–16.

Fang, R.H., Gao, W., Zhang, L., 2023. Targeting drugs to tumors using cell membrane-coated nanoparticles. Nat. Rev. Clin. Oncol. 20 (1), 33–48.

Ferreira, M.P., Ranjan, S., Correia, A.M., Makila, E.M., Kinnunen, S.M., Zhang, H., Shahbazi, M.A., Almeida, P.V., Salonen, J.J., Ruskoaho, H.J., Airaksinen, A.J., Hirvonen, J.T., Santos, H.A., 2016. In vitro and in vivo assessment of heart-homing porous silicon nanoparticles. Biomaterials 94, 93–104.

Ferreira, M.P.A., Ranjan, S., Kinnunen, S., Correia, A., Talman, V., Makila, E., Barrios-Lopez, B., Kemell, M., Balasubramanian, V., Salonen, J., Hirvonen, J., Ruskoaho, H., Airaksinen, A.J., Santos, H.A., 2017. Drug-loaded multifunctional nanoparticles targeted to the endocardial layer of the injured heart modulate hypertrophic signaling. Small 13 (33).

Godin, B., Gu, J., Serda, R.E., Bhavane, R., Tasciotti, E., Chiappini, C., Liu, X., Tanaka, T., Decuzzi, P., Ferrari, M., 2010. Tailoring the degradation kinetics of mesoporous silicon structures through PEGylation. J. Biomed. Mater. Res. A 94 (4), 1236–1243.

Guo, K., Liu, Y., Tang, L., Shubhra, Q.T., 2022. Homotypic biomimetic coating synergizes chemo-photothermal combination therapy to treat breast cancer overcoming drug resistance. Chem. Eng. J. ., 428131120

Gustafson, H.H., Holt-Casper, D., Grainger, D.W., Ghandehari, H., 2015. Nanoparticle uptake: the phagocyte problem. Nano Today 10 (4), 487–510.

He, M., Guo, S., Li, Z., 2015. In situ characterizing membrane lipid phenotype of breast cancer cells using mass spectrometry profiling. Sci. Rep. 5 (1), 1–13.

Jugdaohsingh, R., Tucker, K.L., Qiao, N., Cupples, L.A., Kiel, D.P., Powell, J.J., 2004. Dietary silicon intake is positively associated with bone mineral density in men and premenopausal women of the framingham offspring cohort. J. Bone Miner. Res. 19 (2), 297–307.

Kallinen, A.M., Sarparanta, M.P., Liu, D., Makila, E.M., Salonen, J.J., Hirvonen, J.T., Santos, H.A., Airaksinen, A.J., 2014. In vivo evaluation of porous silicon and porous silicon solid lipid nanocomposites for passive targeting and imaging. Mol Pharm 11 (8), 2876–2886.

Karageorgou, M.-A., Rapsomanikis, A.-N., Mirković, M., Vranješ-Đurić, S., Stiliaris, E., Bouziotis, P., Stamopoulos, D., 2022. ^{99m}Tc-labeled iron oxide nanoparticles as dual-modality contrast agent: a preliminary study from synthesis to magnetic resonance and gamma-camera imaging in mice models. Nanomaterials 12 (15), 2728.

Keinanen, O., Makila, E.M., Lindgren, R., Virtanen, H., Liljenback, H., Oikonen, V., Sarparanta, M., Molthoff, C., Windhorst, A.D., Roivainen, A., Salonen, J.J., Airaksinen, A.J., 2017. Pretargeted PET imaging of trans-cyclooctene-modified porous silicon nanoparticles. ACS Omega 2 (1), 62–69.

Li, M., Fang, H., Liu, Q., Gai, Y., Yuan, L., Wang, S., Li, H., Hou, Y., Gao, M., Lan, X., 2020. Red blood cell membrane-coated upconversion nanoparticles for pretargeted multimodality imaging of triple-negative breast cancer. Biomater. Sci. 8 (7), 1802–1814.

Lila, A.S.A., Kiwada, H., Ishida, T., 2013. The accelerated blood clearance (ABC) phenomenon: clinical challenge and approaches to manage. J. Control. Release 172 (1), 38–47.

Liu, L., Bai, X., Martikainen, M.-V., Kårlund, A., Roponen, M., Xu, W., Hu, G., Tasciotti, E., Lehto, V.-P., 2021a. Cell membrane coating integrity affects the internalization mechanism of biomimetic nanoparticles. Nat. Commun. 12 (1), 1–12.

Liu, Q., Guan, J., Song, R., Zhang, X., Mao, S., 2021b. Physicochemical properties of nanoparticles affecting their fate and the physiological function of pulmonary surfactants. Acta Biomater.

Liu, L., Pan, D., Chen, S., Martikainen, M.-V., Kårlund, A., Ke, J., Pulkkinen, H., Ruhanen, H., Roponen, M., Käkelä, R., 2022. Systematic design of cell membrane coating to improve tumor targeting of nanoparticles. Nat. Commun. 13 (1), 6181.

Lumen, D., Näkki, S., Imlimthan, S., Lambidis, E., Sarparanta, M., Xu, W., Lehto, V.-P., Airaksinen, A.J., 2019. Site-specific ^{111}In-radiolabeling of dual-PEGylated porous silicon nanoparticles and their in vivo evaluation in murine 4T1 breast cancer model. Pharmaceutics 11 (12), 686.

Lumen, D., Wang, S., Mäkilä, E., Imlimthan, S., Sarparanta, M., Correia, A., Haug, C.W., Hirvonen, J., Santos, H.A., Airaksinen, A.J., 2021. Investigation of silicon nanoparticles produced by centrifuge chemical vapor deposition for applications in therapy and diagnostics. Eur. J. Pharm. Biopharm. 158254–215865.

Näkki, S., Rytkönen, J., Nissinen, T., Florea, C., Riikonen, J., Ek, P., Zhang, H., Santos, H. A., Närvänen, A., Xu, W., 2015. Improved stability and biocompatibility of nanostructured silicon drug carrier for intravenous administration. Acta Biomater. 13207–21315.

Park, J.H., Ahn, J.-H., Kim, S.-B., 2018. How shall we treat early triple-negative breast cancer (TNBC): from the current standard to upcoming immuno-molecular strategies. ESMO open 3e000357.

Pellico, J., Gawne, P.J., de Rosales, R.T., 2021. Radiolabelling of nanomaterials for medical imaging and therapy. Chem. Soc. Rev. 50 (5), 3355–3423.

Rahikkala, A., Fontana, F., Bauleth-Ramos, T., Correia, A., Kemell, M., Seitsonen, J., Mäkilä, E., Sarmento, B., Salonen, J., Ruokolainen, J., 2020. Hybrid red blood cell membrane coated porous silicon nanoparticles functionalized with cancer antigen induce depletion of T cells. RSC Adv. 10 (58), 35198–35205.

Riikonen, J., Nissinen, T., Alanne, A., Thapa, R., Fioux, P., Bonne, M., Rigolet, S., Morlet-Savary, F., Aussenac, F., Marichal, C., Lalevée, J., Vepsäläinen, J., Lebeau, B., Lehto, V.-P., 2020. Stable surface functionalization of carbonized mesoporous silicon. Inorg. Chem. Front. 7 (3), 631–641.

Shi, L., Zhang, J., Zhao, M., Tang, S., Cheng, X., Zhang, W., Li, W., Liu, X., Peng, H., Wang, Q., 2021. Effects of polyethylene glycol on the surface of nanoparticles for targeted drug delivery. Nanoscale 13 (24), 10748–10764.

Sun, R., Xiang, J., Zhou, Q., Piao, Y., Tang, J., Shao, S., Zhou, Z., Bae, Y.H., Shen, Y., 2022. The tumor EPR effect for cancer drug delivery: Current status, limitations, and alternatives. Adv. Drug Deliv. Rev., 114614

Sung, H., Ferlay, J., Siegel, R.L., Laversanne, M., Soerjomataram, I., Jemal, A., Bray, F., 2021. Global cancer statistics 2020: GLOBOCAN estimates of incidence and mortality worldwide for 36 cancers in 185 countries. CA Cancer J. Clin. 71 (3), 209–249.

Tamarov, K., Wang, J.-T.-W., Kari, J., Happonen, E., Vesavaara, I., Niemela, M., Peramaki, P., Al-Jamal, K.T., Xu, W., Lehto, V.-P., 2021. Comparison between fluorescence imaging and elemental analysis to determine biodistribution of inorganic nanoparticles with strong light absorption. ACS Appl. Mater. Interfaces 13 (34), 40392–40400.

Tishchenko, V.K., Petriev, V.M., Mikhailovskaya, A.A., Smoryzanova, O.A., Kabashin, A. V., Zavestovskaya, I.N., 2020. Ex vivo biodistribution of gallium-68-labeled porous silicon nanoparticles. J. Phys. Conf. Ser. 1439012035.

Wang, X., Zhong, X., Li, J., Liu, Z., Cheng, L., 2021. Inorganic nanomaterials with rapid clearance for biomedical applications. Chem. Soc. Rev. 50 (15), 8669–8742.

Wen, H., Närvänen, A., Jokivarsi, K., Poutiainen, P., Xu, W., Lehto, V.-P., 2022. A robust approach to make inorganic nanovectors biotraceable. Int. J. Pharm. 624122040.